

Phase engineering of giant second harmonic generation in Bi₂O₂Se

Zhefeng Lou^{1,2,3,†}, Yingjie Zhao^{4,†}, Zhihao Gong^{5,6,†}, Ziye Zhu⁴, Mengqi Wu⁴, Tao Wang¹, Jialu Wang^{7,1}, Haoyu Qi^{8,1}, Huakun Zuo⁹, Zhuokai Xu^{1,2,3}, Jichuang Shen⁴, Zhiwei Wang^{8,10,11}, Lan Li⁴, Shuigang Xu^{1,3}, Wei Kong⁴, Wenbin Li^{4,*}, Xiaorui Zheng^{4,*}, Hua Wang^{5,12,*} & Xiao Lin^{1,3,*}

¹Key Laboratory for Quantum Materials of Zhejiang Province, Department of Physics, School of Science and Research Center for Industries of the Future, Westlake University, Hangzhou 310030, P. R. China.

²School of Physics, Zhejiang University, Hangzhou 310027, Zhejiang Province, China.

³Institute of Natural Sciences, Westlake Institute for Advanced Study, Hangzhou 310024, P. R. China.

⁴Key Laboratory of 3D Micro/nano Fabrication and Characterization of Zhejiang Province, School of Engineering, Westlake University, Hangzhou 310024, Zhejiang Province, P. R. China.

⁵ZJU-Hangzhou Global Scientific and Technological Innovation Center, School of Physics, Zhejiang University, Hangzhou 311215, China.

⁶Academy of Interdisciplinary Studies on Intelligent Molecules, Tianjin Key Laboratory of Structure and Performance for Functional Molecules, College of Chemistry, Tianjin Normal University, Tianjin, 300387, P. R. China.

⁷Hangzhou Key Laboratory of Quantum Matters, School of Physics, Hangzhou Normal University, Hangzhou 311121, China.

⁸Material Science Center, Yangtze Delta Region Academy of Beijing Institute of Technology, Jiaxing 314011, China.

⁹Wuhan National High Magnetic Field Center, Huazhong University of Science and Technology, Wuhan, 430074, China.

¹⁰Centre for Quantum Physics, Key Laboratory of Advanced Optoelectronic Quantum Architecture and Measurement (MOE), School of Physics, Beijing Institute of Technology, Beijing 100081, China.

¹¹Beijing Key Lab of Nanophotonics and Ultrafine Optoelectronic Systems, Beijing Institute of Technology, Beijing 100081, China.

¹²Center for Quantum Matter, Zhejiang University, Hangzhou 310058, China.

These authors contributed equally[†]: Zhefeng Lou, Yingjie Zhao, Zhihao Gong.

*e-mail: liwenbin@westlake.edu.cn (W.L.); zhengxiaorui@westlake.edu.cn

(X.Z.); daodaohw@zju.edu.cn (H.W.); linxiao@westlake.edu.cn (X.L.)

(Dated: July 29, 2024)

Two-dimensional (2D) materials with remarkable second-harmonic generation (SHG) hold promise for future on-chip nonlinear optics. Relevant materials with both giant SHG response and environmental stability are long-sought targets. Here, we demonstrate the enormous SHG from the phase engineering of a high-performance semiconductor, Bi₂O₂Se (BOS), under uniaxial strain. SHG signals captured in strained 20 nm-BOS films exceed those of NbOI₂ and NbOCl₂ of similar thickness by a factor of 10, and are four orders of magnitude higher than monolayer-MoS₂, resulting in a significant second-order nonlinear susceptibility on the order of 1 nm V⁻¹. Intriguingly, the strain enables continuous adjustment of the ferroelectric phase transition across room temperature. Consequently, an exceptionally large tunability of SHG, approximately six orders of magnitude, is achieved through strain or thermal modulation. This colossal SHG, originating from the geometric phase of Bloch wave functions and coupled with sensitive tunability through multiple approaches in this air-stable 2D semiconductor, opens new possibilities for designing chip-scale, switchable nonlinear optical devices.

1. Introduction

Phase transitions can profoundly alter the physical or topological properties of two-dimensional (2D) materials¹⁻⁸, the precise control of which through external stimuli holds significant technological potential across various fields, including electronics, optics, and catalysis⁸⁻¹². Among these, the ferroic phase transition is characterized by the loss of certain point-group symmetries, which holds promise for applications in high-speed non-volatile electronics^{8,13}.

Featuring a narrow bandgap (0.8 eV)¹⁴, high electron mobility^{15,16}, and robust environmental stability¹⁷, the layered semiconductor Bi₂O₂Se (BOS) has become a highly competitive material for next-generation electronics¹⁷⁻²⁰ and broadband optoelectronics²¹⁻²⁵. Our recent work reported local strain engineering of the paraelectric (PE) to ferroelectric (FE) phase transition in BOS²⁶, highlighting BOS as a rare high-performance semicon-

ductor that also exhibits an FE phase transition.

In this work, we discover that phase engineering enables giant second-harmonic generation (SHG) responses in BOS thin films through mechanical/thermal modulations around room temperature (RT). Strikingly, the maximum intensity observed in strained films exhibits a tenfold increase compared to that of NbOX₂ (X=Cl, I) of similar thickness at ambient conditions. The latter has recently received considerable attention due to its huge, thickness scalable SHG²⁷⁻³⁰, as well as excellent spontaneous parametric down-conversion efficiency²⁸. Importantly, the SHG signals in BOS exhibit exceptionally large strain tunability across FE transitions, evolving from below noise levels (i.e. no SHG in the PE phase) at ambient conditions to a value approximately 10⁶ times higher at the strain of $\varepsilon \approx 4.1\%$. Similar behaviour can be achieved by thermal modulation, for which the FE Curie temperature (T_c) is continuously adjusted across

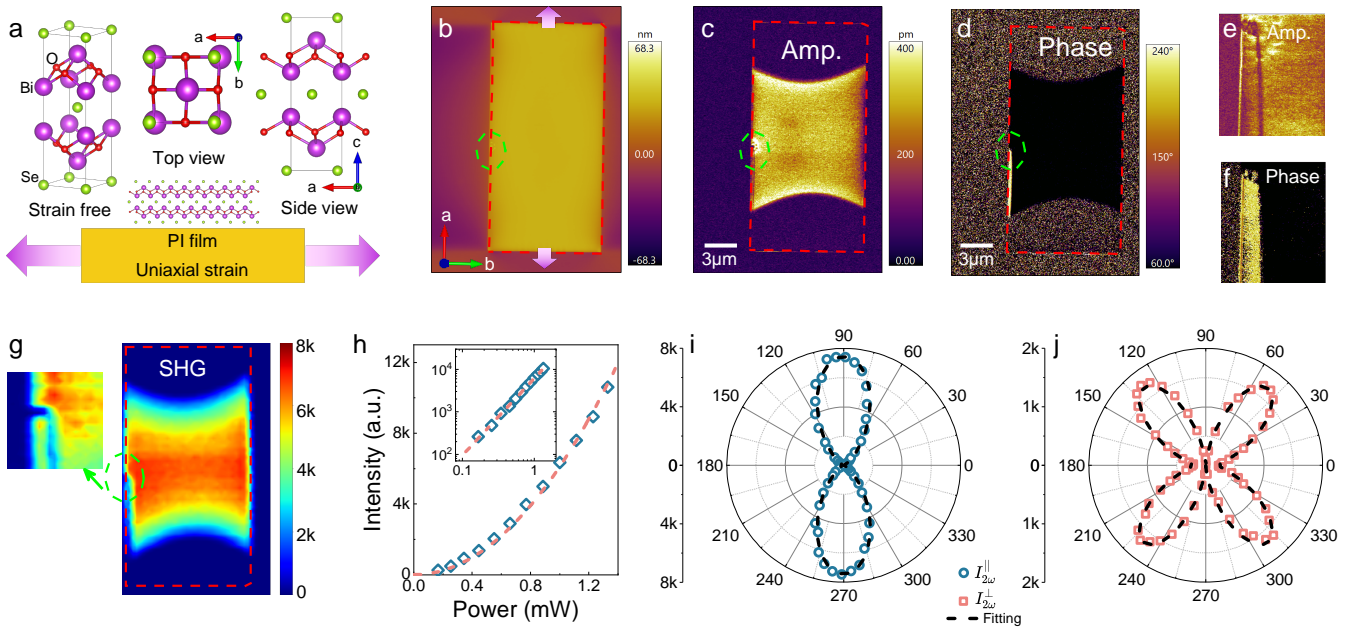


Figure 1. Ferroelectricity in strained BOS. a) Lattice structure of BOS subjected to in-plane uniaxial strain. b) Topography of a strained BOS film from atomic force microscopy. The arrows mark the strain applied along the a -axis (long edge), by sticking BOS to a flexible PI film as sketched in (a). c) Mapping of the in-plane PFM amplitude on the film. d) Mapping of the corresponding phase. e, f) Enlarged images of PFM amplitude and phase, corresponding to the circled area in (b), (c), (d). It illustrates FE domains. g) Mapping of SHG intensity for the same device. The side figure is a magnified image showing FE domains. h) SHG intensity as a function of excitation power. The dashed curve is a quadratic fit. The inset is the same data in a log-log plot. The dashed line is a guide to the eye. i, j) Angular dependence of polarized SHG signals. $I_{2\omega}^{\parallel}$ and $I_{2\omega}^{\perp}$ represent the measurements in the parallel and perpendicular modes, respectively. The dashed curves are fits to the $mm2$ point group, as discussed in Note S1, Supporting Information. The SHG measurements were performed with 1064 nm excitation. All the mapping was measured along the polar-axis as suggested by the maximum in (i). The angle of 90° corresponds to the strain direction. The red dashed boxes outline the specimen.

RT by gradual strain tuning. This level of tunability dramatically exceeds that of other 2D systems subjected to various external stimuli^{2,31–33}. Intriguingly, our first-principles calculations reveal that the geometric phases, such as shift vector, play a crucial role in the SHG response. The remarkable tunability of enormous SHG in BOS films via ferroic phase and geometric phase engineering opens up new possibilities for miniaturized solid-state optical applications, such as quantum light sources, optical modulation and switches, etc^{34,35}.

2. Results and Discussions

2.1 Strain induced ferroelectricity

BOS crystals possess inversion symmetry, adopting a tetragonal anti- ThCr_2Si_2 structure with the $I4/mmm$ space group. Theoretical investigations suggest that the application of uniaxial tensile strain induces a relative in-plane shift between the $[\text{Se}]_n^{2n-}$ and $[\text{Bi}_2\text{O}_2]_n^{2n+}$ layers, as depicted in **Figure 1a**^{36,37}. This disrupts inversion symmetry, leading to a FE transition²⁶. In this study, the strain is achieved by attaching BOS films to stretchable polyimide (PI) substrates. A particular method is employed to enhance the adhesion between the BOS and

PI interface, capable of sustaining strains on BOS films as large as 5% see details in Experimental Section and **Figure S1**, Supporting Information).

Figure 1b-f illustrates piezoelectric force microscopy (PFM) measurements on a strained BOS film. **Figure 1b** is the topography of the rectangular specimen with strain applied along the a -axis. Scanning images of in-plane PFM amplitude and phase are presented in **Figure 1c-d**, which reveal a foresail-like region with distinct contrast to the surroundings. This observation reflects the presence of a FE order in strained BOS²⁶. The relatively weak out-of-plane PFM signal, as shown in **Figure S2**, Supporting Information, further suggests an in-plane FE polarization, aligning well with density functional theory (DFT) calculations^{36,37}.

Interestingly, a domain wall structure, extending from a point defect at the edge (enclosed by a circle), is detected in **Figure 1c-d**. The enlarged image in **Figure 1e-f** reveals two distinct regimes, separated by a line boundary, with identical PFM amplitude but 180° out of phase. Notably, this boundary does not correspond to a strain-induced fracture, as evidenced by the topography of the specimen. Moreover, the domain walls exhibit adjusta-

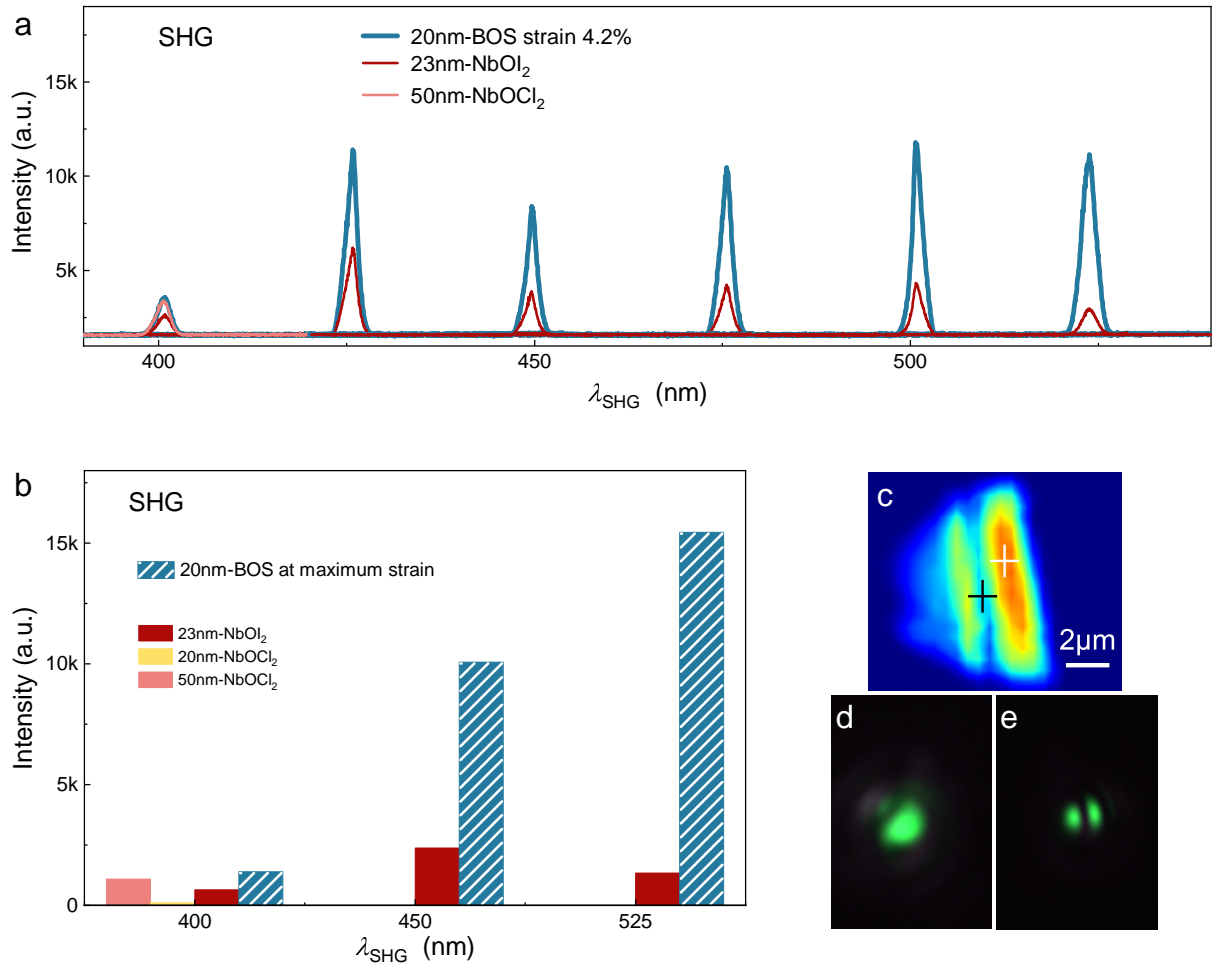


Figure 2. Giant SHG in a strained BOS film with a thickness of 20 nm. a) SHG intensity for strained BOS ($\varepsilon \approx 4.2\%$) at different wavelengths. b) Maximum SHG of BOS at selective wavelengths ($\lambda_{\text{SHG}} = 400, 450$ and 525 nm) recorded prior to the film rupture under tension. In (a) and (b), strain-free 23 nm-NbOI₂, 20 nm-NbOCl₂ and 50 nm-NbOCl₂ were employed as control samples. c) Mapping of SHG intensity near a domain boundary for strained BOS. d,e) Optical images of SHG emission located inside a domain (white ‘+’ in (c)) and at the domain wall (black ‘+’), respectively. They are recorded in a confocal microscope with 1064 nm excitation. The spot size is about $1 \mu\text{m}^2$.

bility based on the history of strain application, as seen in Figure S3, Supporting Information. All these indicate the presence of FE domain structure in strained BOS.

Figure 1g-j presents the primitive SHG measurement on the same device. In Figure 1g, the SHG intensity mapping revealed a foresail-like region of enhanced SHG responses as well as a domain wall structure, which appears to be identical to that detected by PFM, underscoring the intimacy between SHG and the FE phase. In Figure 1h, the SHG signals exhibit a typical scaling with the square of excitation power. Moreover, in Figure 1i and j, the angle-dependence of polarization signals detected in the parallel- $I_{2\omega}^{\parallel}$ and perpendicular- $I_{2\omega}^{\perp}$ modes follows a twofold rotational symmetry from the predicted $mm2$ point group in the FE phase of strained BOS²⁶. In Figure 1i, the maximum at 90° corresponds to the polar axis aligned with the strain (a -axis), as expected by DFT calculations³⁶. Details of the measurements are pre-

sented in Experimental Section; Figure S4 and Note S1, Supporting Information.

Note that the polar signals are observed only in the central foresail-like region, rather than across the whole sample. This observation aligns well with the simulated strain distribution on BOS films as seen in Figure S5-S7, Supporting Information, where the strain transferred from the PI substrates shows moderate non-uniformity, with higher ε in the middle and lower ε on either side. The curved edges that separate the polar/non-polar regions in Figure 1c,d,g, correspond to $\varepsilon = \varepsilon_c$ ^{26,36-38}. It is important to emphasize that flexoelectricity induced by the non-uniform strain is negligible in contributing to the observed signals, as detailed in Figure S6 and Note S2, Supporting Information.

2.2 Giant SHG

Figure 2a illustrates the wavelength dependence of SHG

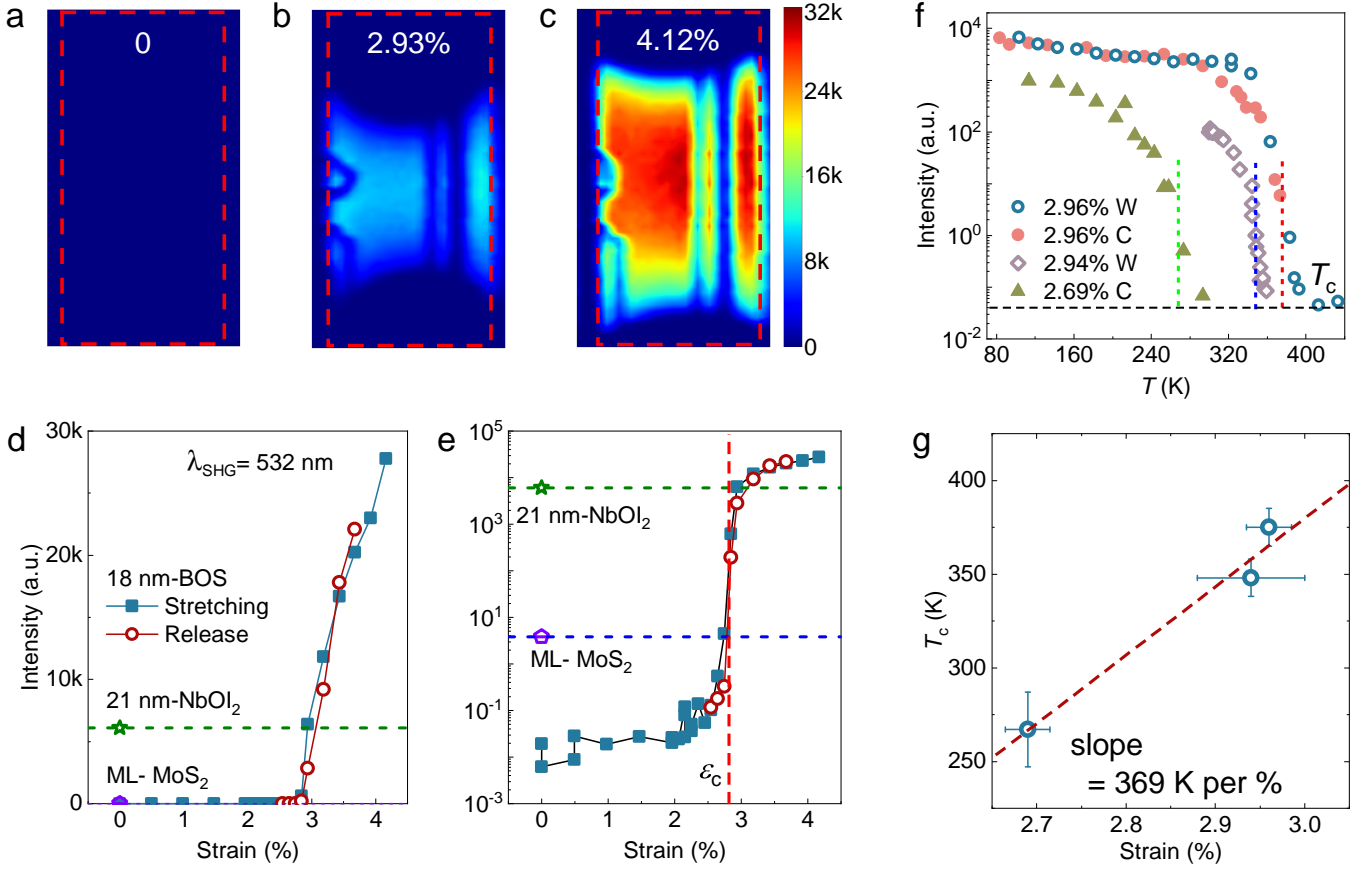


Figure 3. Multiple modulations of SHG. a-c) SHG mapping for BOS at strains below (0), around (2.93%) and above (4.12%) ϵ_c of the FE transition. The dashed boxes outline the BOS film. The mapping was measured along the polar axis. Please refer to Figure S11, Supporting Information, for the mapping along the non-polar axis, where SHG signals are negligible as strain varies. d,e) Mechanical modulation of SHG intensity across the FE transition at RT. The data is plotted in linear and semi-log scale, respectively. 21 nm-NbOI₂ and ML-MoS₂ were employed as control samples. f) Thermal modulation of SHG intensity at different strains around RT. The vertical dashed lines mark the FE Curie temperature, determined at the peak of the first derivative. ‘C’/‘W’ denotes cooling/warming. g) Strain modulation of T_c . The dashed line is a linear fit. The error bars indicate uncertainties in determination of extracted values. The data was collected via 1064 nm excitation along the polar axis.

intensity for a 20 nm-thick BOS film under substantial uniaxial strain ($\epsilon \approx 4.2\%$), with λ_{SHG} spanning from 400 nm to 525 nm. It is compared with the data simultaneously obtained on a well-established 2D NbOX₂ system, specifically, 23 nm-NbOI₂ and 50 nm-NbOCl₂. Surprisingly, the strained BOS shows a higher SHG intensity than NbOX₂ films of similar thickness across the whole wavelength range measured. Consequently, we further stretch the BOS film and measure the SHG intensity at selected λ_{SHG} . In Figure 2b, the maximum SHG, recorded at $\epsilon > 5\%$ (just before the fracture of the sample), is compared with NbOX₂ at the characteristic wavelengths chosen in two seminal papers^{27,28}. The SHG response of 20 nm-BOS is approximately an order of magnitude larger than that of 23 nm-NbOI₂ at $\lambda_{\text{SHG}} = 525 \text{ nm}$ and than that of 20 nm-NbOCl₂ at $\lambda_{\text{SHG}} = 400 \text{ nm}$ (see Raman characterization in Figure S8, Supporting

Information).

Given the second-order nonlinear susceptibility ($\chi^{(2)}$) of NbOI₂ and NbOCl₂ in Table S1^{27,28}, Supporting Information, a significant $\chi^{(2)}$ on the order of 1 nm V⁻¹ is inferred for strained BOS (see detailed calculations in Note S3 and Figure S9, S10, Supporting Information). It is more than one order of magnitude higher than that of LiNbO₃ (0.04 nm V⁻¹)³⁹ and among the highest value of 2D materials, including transition metal dichalcogenides (TMDCs)^{40,41}. While in TMDCs, the odd-even layer selectivity combined with the inter-layer coupling impedes the thickness scalability of SHG response^{34,35,42}. For example, the 3R-MoS₂ requires a much greater thickness ($\sim 700 \text{ nm}$) to achieve a giant SHG response⁴³. Similarly, comparable thicknesses are also needed for r-BN and BN nanotubes (BNNT) due to their small $\chi^{(2)}$ values ($\chi_{\text{r-BN}}^{(2)} \sim 0.03 \text{ nm V}^{-1}$,

$\chi_{\text{BNNT}}^{(2)} \sim 0.05 \text{ nm V}^{-1}$)^{44,45}. Further comparison of $\chi^{(2)}$ with other systems is included in Table S2, Supporting Information. In Figure 2d and e, we observe a remarkable SHG emission from the BOS films directly on the camera of a confocal microscope (see details in Experimental Section). The spots in two figures differ in shape, which is intrinsic to the SHG response to the location of domain bulk and domain walls, as seen in the SHG mapping of Figure 2c. Here, we achieve the first major outcome of present work, which may expand the functionality of the high-performance semiconductor BOS and motivate multiple applications in on-chip optical parametric oscillators and optical transistors^{46–48}.

2.3 Multiple modulation of SHG response.

In the following, we investigate the substantial mechanical and thermal modulation of SHG intensity on a 18 nm-BOS device. The measurements were performed at $\lambda_{\text{SHG}} = 532 \text{ nm}$ in a commercial instrument. **Figure 3a-c** depict the spatial distribution of SHG, demonstrating the variation of SHG intensity under three representative strains at RT. At $\varepsilon = 0$, no SHG signal is detected, consistent with the PE phase at ambient conditions. This observation also rules out the possible SHG contribution from the PI-BOS or BOS-air interface that naturally lacks inversion symmetry. While, at $\varepsilon \approx 2.93\%$, discernible SHG appears in the central region of the sample, indicating the transition from the PE to FE phase. Upon further stretching the device to $\varepsilon \approx 4.2\%$, the SHG intensity significantly strengthens. In Figure 3c, the SHG mapping also reveals multiple FE domain boundaries, primarily along the strain direction, which are absent in the optical image of Figure S11a, Supporting Information. Since the polarizations of neighboring domains both align with the strain, these boundaries are generally neutral 180° domain walls.

Figure 3d illustrates the evolution of SHG intensity as the strain varies, employing 21 nm-NbOI₂ and a CVD-grown 1H-MoS₂ monolayer (ML) as control samples. Notably, data from both stretching and release processes nearly collapse, indicating negligible relaxation during the strain transfer from PI to BOS even at $\varepsilon > 4\%$. This underscores the robust adhesion at the interface, a crucial factor in maintaining structural integrity in strain engineering (see more in Figure S7, Supporting Information). This reversibility ensures a predictable SHG response within repetitive strain cycling, a critical feature for nonlinear optical modulators². In the figure, the critical strain $\varepsilon_c \approx 2.8(1)\%$ is clearly resolved, above which I_{SHG} exhibits pronounced enhancement, surpassing that of NbOI₂ by a factor of 4.6 at $\varepsilon \approx 4.2\%$, with no trend of saturation observed. Similar observations at other wavelengths are presented in Figure S12, Supporting Information. The observed ε_c is close to the critical value of the PE-FE transition calculated in ref. 37. It's noteworthy that the strain in BOS can be fixed using epoxy resin, and Figure S13, Supporting Information demonstrates the environmental robustness of its SHG response over

seven months. In contrast, NbOX₂ is less stable under ambient conditions^{28,49}.

In Figure 3e, the same data, presented in a semi-log plot, highlights the exceptionally large tunability of I_{SHG} . I_{SHG} evolves from the noise level (no SHG) at zero strain to a value six orders of magnitude higher at $\varepsilon \approx 4.2\%$ (approximately 10^4 times that of ML-MoS₂). In particular, the strain demonstrates a significant tunability of I_{SHG} within a narrow strain range around ε_c , i.e. a tunability of I_{SHG} by a factor of 10^4 within $\Delta\varepsilon \approx 0.3\%$. Now, let's delve into the thermal modulation of SHG in BOS by adjusting the strain to bring T_c of the FE transition close to RT. Figure 3f shows the T -evolution of SHG around RT at selective strains. As T lowers, I_{SHG} undergoes a steep rise corresponding to the PE to FE transition, resulting in a significant variation of five orders of magnitude. In Figure 3g, T_c is roughly linear with strain, exhibiting sensitive tunability evolving from $T_c \approx 267 \text{ K}$ at $\varepsilon \approx 2.69\%$ to 375 K at 2.96% , corresponding to a large average slope $dT_c/d\varepsilon \approx 369 \text{ K per } \%$. The dramatic tunability of both I_{SHG} and T_c in the vicinity of RT renders BOS highly valuable for advanced nonlinear optical signal processing based on mechano-optical or thermo-optical modulators^{50–52}. These results represent the second major outcome of this work.

2.4 Microscopic origin and geometric aspects

Our experimental findings strongly indicate a close relationship between the pronounced SHG response and the FE phase transition in strain-modulated BOS. To gain a microscopic understanding of the SHG response, we performed first-principles calculations of the SHG susceptibility χ^{ijk} . **Figure 4a** shows the calculated spectrum of the major component ($|\chi^{\text{aaa}}|$) for BOS under various strains ($\varepsilon > \varepsilon_c$). Its comparison with the minor components is shown in Figure S14 and S15, Supporting Information. The spectrum exhibits significant values across a broad wavelength range, with four distinct peaks (labeled A-D) between 310 nm and 830 nm. We propose that our experimental SHG response originates from the spectral region around Peak-B, highlighted by the vertical lines in Figure 4a. In this region, $|\chi^{\text{aaa}}|$ approaches a value of approximately 1 nm V^{-1} , in close agreement with our experimental results. The strain dependence of $|\chi^{\text{aaa}}|^2$ ($\sim I_{2\omega}$, see Note S3, Supporting Information) at 459.2 nm (around Peak-B) and the planar angular anisotropy of total SHG intensity are presented in Figure 4b and c, respectively. Above ε_c ($\sim 3\%$), a significant enhancement in $|\chi^{\text{aaa}}|^2$ and a two-fold rotational symmetry, preserved for various strains, are observed. These theoretical predictions agree quantitatively with our experimental findings in Figure S12, Supporting Information.

Figure 4d illustrates the calculated band structure of BOS at $\varepsilon = 5\%$. The valence bands near the gap (v_1 and v_2) arise from Se-4p orbitals, while the conduction bands (c_1 and c_2) come from Bi-6p orbitals. Deeper valence bands are attributed to O-2p orbitals. The double-

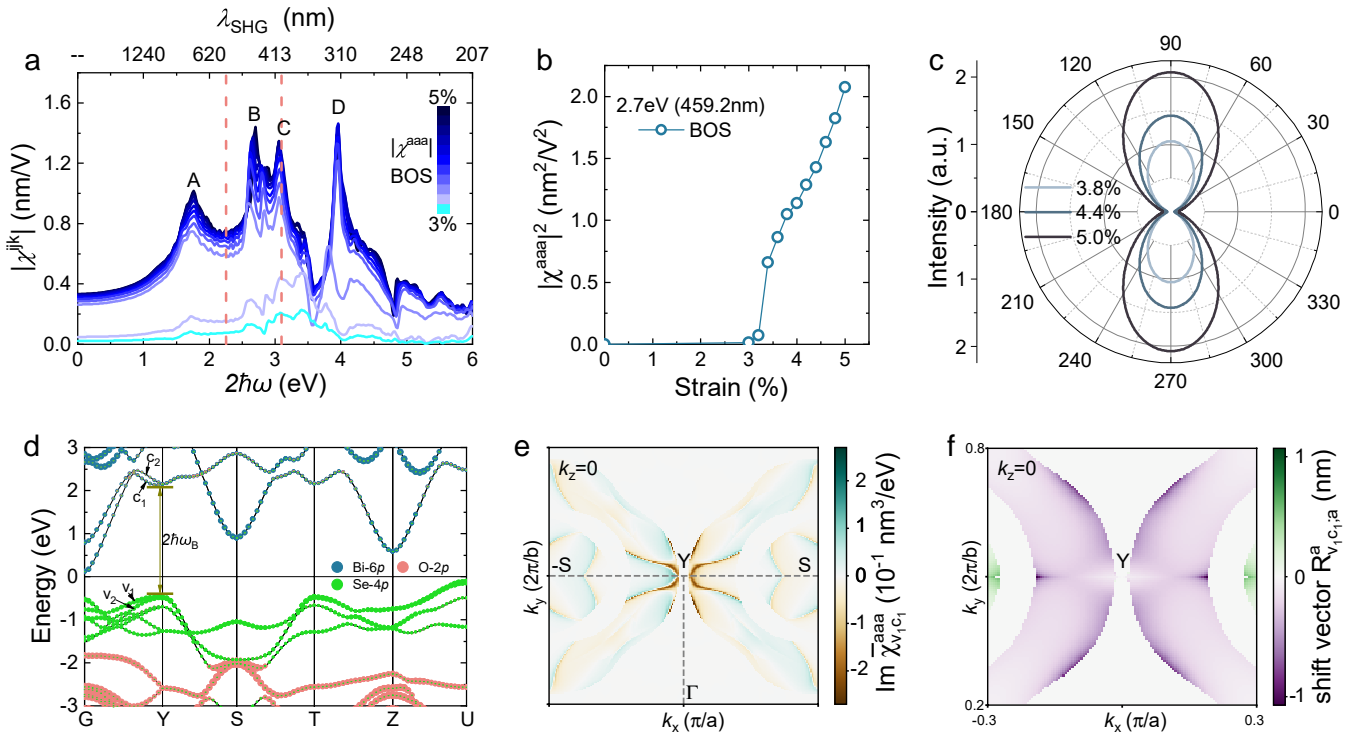


Figure 4. First-principles calculations of SHG. a) Calculated nonlinear susceptibilities $|\chi^{\text{aaa}}|$ of strained BOS, ranging from $\varepsilon = 3\%$ (light blue) to 5% (dark blue), at a strain step of 0.2% . a is the polar axis. Four peaks (A-D) of the SHG response are resolved. Two vertical dashed lines enclose the frequency range of our measurement. b) Calculated mechanical modulation of $|\chi^{\text{aaa}}|^2$ for BOS, with the SHG photon energy of 2.7 eV (around Peak-B). c) Angle-dependence of calculated total SHG intensities (see the definition in Note S1, Supporting Information) at different strains. d) Band structure of BOS at $\varepsilon = 5\%$. The projections of Bi- $6p$, O- $2p$, and Se- $4p$ orbitals are highlighted with the size of circles indicating their weight in the bands. e) (k_x, k_y) distribution of the representative (v_1, c_1) -band contributions to SHG, $\text{Im}[\bar{\chi}_{v_1c_1}^{\text{aaa}}]$. f) Corresponding distribution of the shift vector $R_{v_1c_1;a}^a$. The (k_x, k_y) heatmap is constructed at $k_z = 0$ for Peak-B at $\varepsilon = 5\%$.

photon resonant transition between v_1 and c_1 around the high-symmetry Y -point coincides with Peak-B in the spectrum. The relatively less dispersive bands around Y leads to higher density of states (DOS) and increased absorbance near the gap in Figure S16, Supporting Information. This consequently triggers strong nonlinear response around Y -point with the major contribution from the (v_1, c_1) transition, as seen in Figure 4e, which illustrates the distribution of SHG susceptibility within the (k_x, k_y) -plane at $k_z = 0$ at $\varepsilon = 5\%$ (see more discussions associated with other strains in Figure S17-S20, Supporting Information).

As shown in Figure S21, Supporting Information, the significant strain tunability of SHG in BOS primarily arises from the strain sensitivity of the “shift” component ($\chi_{\text{shift}}^{\text{aaa}}$) of the total SHG susceptibility. This term dominates the contribution over the “triple” and “inject” components and is associated with the geometric quantity termed the shift vector $R_{nm;a}^a$, which elucidates the spatial displacement of charge centers along the a -direction upon a -polarized photon absorption with n, m the band index. Figure 4f presents the distribution of $R_{v_1c_1;a}^a$ around Y -point, corresponding to the region of

the most pronounced SHG susceptibility in Figure 4e. The similar profiles in two figures highly suggest the dominant role of geometric shift vector in inducing the SHG susceptibility around Peak-B.

Notably, $R_{nm;a}^a$ is related to the electronic part of FE polarization since both are proportional to the intra-band Berry connection A_n^a (see details in Note S4, Supporting Information). As depicted in Figure S22, Supporting Information, a finite distribution of $R_{v_1c_1;a}^a$ around Y -point emerges once the strain-induced FE distortion disrupt the inversion symmetry at $\varepsilon > 3\%$. Its overall magnitude increases with strain, correlated with the substantial enhancement in the (v_1, c_1) -band contribution to the SHG susceptibility as detailed in Figure S18 and S19, Supporting Information. Therefore, understanding the evolution of the electronic geometric phase are crucial for explaining the giant SHG observed in BOS during the FE phase transition.

3. Conclusion

Our work demonstrates giant and exceptionally tunable SHG in BOS nanosheets through the strain or thermal modulation of FE phase transition. A deep connection

between the giant SHG, the FE phase transition, and the geometric phase of the electrons is also revealed, imparting a new meaning to the concept of phase engineering by encompassing both the FE phase and the geometric phase. The unprecedented tunability of the SHG responses in BOS near RT, coupled with the environmental stability and other attractive electronic and optoelectronic properties of BOS^{17,18,21–23}, may open the route towards a variety of applications involving highly sensitive, switchable nonlinear optics^{29,50,51}. The interplay between the geometric phases of electrons and ferroic phase transitions may also open new avenues to explore emerging physics as well as unexpected functionalities in conventional and novel materials, which is of paramount interest for future research.

4. Experimental Section

Sample Growth: Inclined BOS nanosheets were synthesized via the physical vapor deposition (PVD) method, utilizing Bi₂O₃ powder (99.99%, Aladdin) and BOS single crystals as precursors. These precursors are placed at the heating center of a horizontal oven and heated to 740 °C. High purity argon was employed as the gas agent to deliver the precursors onto fluorophlogopite mica at a flow rate of 100 – 200 sccm and pressure of 380 Torr. The mica was positioned at 10 – 13 cm downstream of the precursors. This reaction lasted for 10 minutes, after which the oven was naturally cooled down to room temperature, resulting in the formation of inclined BOS nanosheets.

Bulk NbOX₂ single crystals were synthesized using the chemical vapor transport (CVT) method as previously reported^{27,28}. For NbOI₂, high-purity (5N) Nb and Nb₂O₅ powders were mixed together with I₂ flakes in a molar ratio of 3 : 1 : 5 as source materials. For NbOCl₂, high purity Nb, Nb₂O₅ and NbCl₅ (5N) powders were mixed in stoichiometric ratio. They were then loaded into a 22 cm long quartz ampoule and sealed under high vacuum ($< 10^{-2}$ Pa). The ampoule was placed in a dual-zone horizontal oven. The oven was then heated from RT to 873 K over 1 day and held at this temperature for 5 days. Subsequently, one end of the ampoule containing raw materials was cooled to 583 K at a rate of 1.2 K/h, while the opposite end was cooled to 513 K at a rate of 1.5 K/h. The resulting single crystals were millimetres in size with a lustrous appearance. NbOX₂ single crystals were stored in an N₂-filled glove box to prevent deliquescence. Thin films of NbOCl₂ and NbOI₂ were obtained by mechanical exfoliation of single crystals onto SiO₂/Si and quartz substrates, respectively.

1H-ML MoS₂ were grown on sapphire (0001) substrates by low pressure chemical vapor deposition (CVD) under S-rich conditions⁵³. Elemental S powder (99.95%, Aladdin) and MoO₃ powder (99.95%, Alfa Aesar) were used as the sulfur and molybdenum sources, respectively. Prior to growth, the substrates were subjected to low pressure annealing at 1000 °C for 4 hours under a 400

sccm Ar and 100 sccm O₂ gas flow.

Strain engineering: The devices for strain engineering were fabricated by transferring BOS nanosheets onto a stretchable polyimide (PI) film. To ensure robust adhesion at the interface between BOS and PI, a specific process was employed as follows: First of all, 15% polyamic acid solution was spin-coated onto the surface of PI substrate (50 μm) at a speed of 3000 rpm for 1 min, followed by baking at 70 °C for 24 h to remove the dimethylacetamide solvent. Second, inclined BOS nanosheets were transferred onto the substrate prepared in the first step using a tip-assisted transfer method⁵⁴. Finally, the device was heated at 180 °C for 30 min to polymerize the polyamic acid into PI. During the polymerization process, a strong adhesion was formed at the interface, ensuring effective strain transfer from PI substrates to BOS films. The in-plane uniaxial strain was applied using a homemade stretching apparatus, as shown in Figure S1, Supporting Information.

This method enables much larger strains on the nanosheets compared to techniques that directly transfer 2D nanosheets onto flexible substrates^{31,55–57}. As in our experiment, we did not observe any strain relaxation phenomena, such as wrinkling⁵⁸ or slippage⁵⁹, even when the strain on BOS exceeded 5%. It appears that the maximum strain is only limited by the quality of target films as evidenced by the film rupture under strain, rather than the interaction strength between BOS and substrates. This technique may have broader applications in the field of strain engineering for other 2D systems. We note that a PVA-assisted strain transfer technique could also achieve considerable strain on MoS₂ by bending, which differs from our approach. For further details, please refer to ref. 60.

PFM measurements: PFM measurements were conducted using a vector-PFM modulus in a Jupiter XR atomic force microscope. Pr/Ir-coated tips with a radius of < 25 nm and a spring constant of about 2 N/m were utilized as probes. The out-of-plane PFM signal was recorded by detecting the deflection of cantilever, while the in-plane signal was captured by the torsion of cantilever, which correlates with the in-plane deformation. Throughout the measurements, the cantilever was positioned perpendicular to the polar axis.

SHG measurements: The measurements in Figure 1, 2c,d and 3 were conducted using the reflection geometry of a confocal microscope (WITec, Alpha300RAS) equipped with a 1064 nm laser excitation source (NPI Rainbow 1064 OEM) with a pulse duration of 8.4 ps and a repetition rate of 50 MHz. The excitation beam was focused onto the sample with a spot size of approximately 1 μm² using a ×100 objective lens with a numerical aperture (NA) of 0.75 for measurements at RT. To improve the resolution for small SHG signals in BOS

under low strains and ML-MoS₂, both laser power and integration time were increased. For comparative analysis, the SHG signals in Figure 3d and e were normalized to a value calculated assuming $P = 1.38$ mW and $\tau = 0.1$ s, since SHG intensity exhibits a linear relationship with the square of power and integration time ($\bar{I}_{\text{SHG}} = I_{\text{SHG}}(P, \tau) \frac{1.38 \text{ mW} \cdot 0.1 \text{ s}}{P^2 \cdot \tau}$). This normalization ensures the accurate comparison across different experimental conditions. In Figure 3f, T -dependent SHG signals were collected using a continuous-flow optical microscopy cryostat (Linkam THM600 stage) with a $\times 50$ objective lens (NA = 0.55). Similar to previous measurements, the intensity was normalized to facilitate comparative analysis across different temperatures. T_c and ε_c were determined from the peak of the first derivative of the semi-log plots in Figure 3e,f. In Figure 2c,d, the optical image are recorded by a CMOS camera (Imaging Source) with an excitation power (P) of 9.7 mW.

The measurements in Figure 2a and b were carried out in a homemade system with a reflection geometry. Here, a femtosecond laser (Light Conversion, PHAROS PH2-10W) was utilized to pump the optical parametric amplifier (Light Conversion, ORPHEUS-F, pulse duration of 180 fs, repetition rate of 10 kHz) to generate laser beams of wavelengths ranging from 800 nm to 1100 nm in steps of 50 nm. The incident beam was directed through an $\times 40$ objective lens (Olympus, RMS40X-PF, NA=0.75) and focused onto the samples with a spot radius of approximately 1.5 μm . Due to the reflection geometry, the outgoing SHG signal was captured by the same objective and analyzed by an imaging spectrometer (Princeton Instruments, IsoPlane SCT 320). During the measurements, the excitation laser power was carefully maintained at 5 μW , as monitored by a silicon photodiode power sensor (Thorlabs, S130C).

First-principles calculations: The Kohn-Sham electronic structure of optimized crystal configuration was achieved by performing density functional theory (DFT) calculations^{61,62} using the Vienna *Ab initio* Simulation Package (VASP)^{63,64} code. The exchange-correlation energy of valence electrons was treated by the generalized gradient approximated (GGA) functionals^{65,66} of Perdew-Burke-Ernzerhof (PBE) type parameterization⁶⁷. An energy cutoff for the plane-wave basis was set to 400 eV, with a $9 \times 9 \times 3$ Monkhorst-Pack k -point sampling. Convergence was reached when residual forces in ion relaxation were below 10^{-3} eV/Å and the energy difference between sequential steps of electronic self-consistent field calculation was less than 10^{-6} eV. For the efficient evaluation of SHG susceptibility, the Hamiltonian was obtained using the Wannier tight-binding method⁶⁸⁻⁷⁰ implemented in the Wannier90 code⁷¹. In the Wannier tight-binding calculations, a dense k -point mesh of $100 \times 100 \times 40$ for

converged integrals of the Brillouin zone and an energy width of $\eta = 0.025$ eV for smearing Dirac δ -functions were adopted.

Supporting Information

Supporting Information is available from the author.

Acknowledgments

This research is supported by “Pioneer” and “Leading Goose” R&D Program of Zhejiang under Grant 2024SDXHDX0007, Zhejiang Provincial Natural Science Foundation of China for Distinguished Young Scholars under Grant No. LR23A040001 and the Research Center for Industries of the Future (RCIF) at Westlake University under Award No. WU2023C009 and WU2022C024. W.L. acknowledges the support by NSFC under Award No. 62374136. H.W. acknowledges the support provided by NSCF under Grant No. 12304049. X.Z. acknowledges the support by Westlake Institute For OptoElectronics. We thank the support provided by Lin Liu from Instrumentation and Service Center for Physical Sciences (IS-CPS) and Zhong Chen for Molecular Sciences (ISCMS) at Westlake University.

Author contributions

Z.L., Y.Z. and Z.G. contributed equally to this work. Z.L. fabricated the device and performed PFM measurements with the assistance of M.W., H.Q., H.Z., Z.X. and L.L.. Z.L. and Y.Z. did optical measurements supervised by X.Z. and X.L.. Z.G. and Z.Z. did DFT calculations supervised by W.L. and H.W.. T.W. grew BOS nanosheets. J.S., W.K. and S.X. offered high-quality ML-MoS₂. J.W. offered NbOI₂ single crystals. Z.W. offered NbOCl₂ single crystals. Z.L., Z.G. and X.L. prepared the figures. W.L., H.W. and X.L. wrote the paper with the inputs from Z.L. and Z.G.. X.L. led the project. All authors contributed to the discussion.

Conflict of Interest

The authors declare no conflict of interest.

Data Availability Statement

The data that support the findings of this study are included in this article and its supplementary information file and are available from the corresponding author upon reasonable request.

Keywords

bismuth oxyselenide, second harmonic generation, ferroelectric transition, strain engineering

[1] Yasuda, K., Wang, X., Watanabe, K., Taniguchi, T. & Jarillo-Herrero, P. Stacking-engineered ferroelectricity in

bilayer boron nitride. *Science* **372**, 1458–1462 (2021).

- [2] Wang, Y. *et al.* Structural phase transition in monolayer MoTe₂ driven by electrostatic doping. *Nature* **550**, 487–491 (2017).
- [3] Zhang, F. *et al.* Electric-field induced structural transition in vertical MoTe₂-and Mo_{1-x}W_xTe₂-based resistive memories. *Nat. Mater.* **18**, 55–61 (2019).
- [4] Yang, H., Kim, S. W., Chhowalla, M. & Lee, Y. H. Structural and quantum-state phase transitions in van der Waals layered materials. *Nat. Phys.* **13**, 931–937 (2017).
- [5] Ghiotto, A. *et al.* Quantum criticality in twisted transition metal dichalcogenides. *Nature* **597**, 345–349 (2021).
- [6] Cho, S. *et al.* Phase patterning for ohmic homojunction contact in MoTe₂. *Science* **349**, 625–628 (2015).
- [7] Yang, X. *et al.* Commensurate stacking phase transitions in an intercalated transition metal dichalcogenide. *Adv. Mater.* **34**, 2108550 (2022).
- [8] Li, W., Qian, X. & Li, J. Phase transitions in 2D materials. *Nat. Rev. Mater.* **6**, 829–846 (2021).
- [9] Wang, R. *et al.* Strategies on phase control in transition metal dichalcogenides. *Adv. Funct. Mater.* **28**, 1802473 (2018).
- [10] Voiry, D., Mohite, A. & Chhowalla, M. Phase engineering of transition metal dichalcogenides. *Chem. Soc. Rev.* **44**, 2702–2712 (2015).
- [11] Sie, E. J. *et al.* An ultrafast symmetry switch in a Weyl semimetal. *Nature* **565**, 61–66 (2019).
- [12] Liu, X. *et al.* On-device phase engineering. *Nat. Mater.* (2024).
- [13] Wu, M. & Li, J. Sliding ferroelectricity in 2D van der Waals materials: Related physics and future opportunities. *PNAS* **118**, e2115703118 (2021).
- [14] Chen, C. *et al.* Electronic structures and unusually robust bandgap in an ultrahigh-mobility layered oxide semiconductor, Bi₂O₂Se. *Sci. Adv.* **4**, eaat8355 (2018).
- [15] Wu, J. *et al.* High electron mobility and quantum oscillations in non-encapsulated ultrathin semiconducting Bi₂O₂Se. *Nat. Nanotechnol.* **12**, 530–534 (2017).
- [16] Zhang, C. *et al.* Single-crystalline van der Waals layered dielectric with high dielectric constant. *Nat. Mater.* **22**, 832–837 (2023).
- [17] Li, T. & Peng, H. 2D Bi₂O₂Se: An emerging material platform for the next-generation electronic industry. *Acc. Mater. Res.* **2**, 842–853 (2021).
- [18] Tan, C. *et al.* 2D fin field-effect transistors integrated with epitaxial high-k gate oxide. *Nature* **616**, 66–72 (2023).
- [19] Zhang, Y. *et al.* A single-crystalline native dielectric for two-dimensional semiconductors with an equivalent oxide thickness below 0.5 nm. *Nat. Electron.* **5**, 643–649 (2022).
- [20] Li, T. *et al.* A native oxide high- κ gate dielectric for two-dimensional electronics. *Nat. Electron.* **3**, 473–478 (2020).
- [21] Khan, U. *et al.* Controlled vapor–solid deposition of millimeter-size single crystal 2D Bi₂O₂Se for high-performance phototransistors. *Adv. Funct. Mater.* **29**, 1807979 (2019).
- [22] Tong, T. *et al.* Sensitive and ultrabroadband phototransistor based on two-dimensional Bi₂O₂Se nanosheets. *Adv. Funct. Mater.* **29**, 1905806 (2019).
- [23] Fu, Q. *et al.* Ultrasensitive 2D Bi₂O₂Se phototransistors on silicon substrates. *Adv. Mater.* **31**, 1804945 (2019).
- [24] Yin, J. *et al.* Ultrafast and highly sensitive infrared photodetectors based on two-dimensional oxyselenide crystals. *Nat. Commun.* **9**, 3311 (2018).
- [25] Chen, Y. *et al.* Momentum-matching and band-alignment van der Waals heterostructures for high-efficiency infrared photodetection. *Sci. Adv.* **8**, eabq1781 (2022).
- [26] Wu, M. *et al.* Achieving ferroelectricity in a centrosymmetric high-performance semiconductor by strain engineering. *Adv. Mater.* **35**, 2300450 (2023).
- [27] Abdelwahab, I. *et al.* Giant second-harmonic generation in ferroelectric NbOI₂. *Nat. Photon.* **16**, 644–650 (2022).
- [28] Guo, Q. *et al.* Ultrathin quantum light source with van der Waals NbOCl₂ crystal. *Nature* **613**, 53–59 (2023).
- [29] Ye, L. *et al.* Manipulation of nonlinear optical responses in layered ferroelectric niobium oxide dihalides. *Nat. Commun.* **14**, 5911 (2023).
- [30] Fu, T. *et al.* Manipulating Peierls distortion in van der Waals NbOX₂ maximizes second-harmonic generation. *J. Am. Chem. Soc.* **145**, 16828–16834 (2023).
- [31] Wang, H. *et al.* Anisotropic strain-tailoring nonlinear optical response in van der Waals NbOI₂. *Nano Lett.* **24**, 3413–3420 (2024).
- [32] Seyler, K. L. *et al.* Electrical control of second-harmonic generation in a WSe₂ monolayer transistor. *Nat. Nanotechnol.* **10**, 407–411 (2015).
- [33] Wang, Y. *et al.* Direct electrical modulation of second-order optical susceptibility via phase transitions. *Nat. Electron.* **4**, 725–730 (2021).
- [34] Autere, A. *et al.* Nonlinear optics with 2D layered materials. *Adv. Mater.* **30**, 1705963 (2018).
- [35] Zhang, J., Zhao, W., Yu, P., Yang, G. & Liu, Z. Second harmonic generation in 2D layered materials. *2D Mater.* **7**, 042002 (2020).
- [36] Wu, M. & Zeng, X. C. Bismuth oxychalcogenides: A new class of ferroelectric/ferroelastic materials with ultra high mobility. *Nano Lett.* **17**, 6309–6314 (2017).
- [37] Zhu, Z., Hu, J., Yao, X. & Zhao, S. Quadruple-well ferroelectricity and topological domain structures in strained Bi₂O₂Se. *J. Mater. Chem. C* **12**, 5951–5957 (2024).
- [38] Zhu, Z., Yao, X., Zhao, S., Lin, X. & Li, W. Giant modulation of the electron mobility in semiconductor Bi₂O₂Se via incipient ferroelectric phase transition. *J. Am. Chem. Soc.* **144**, 4541–4549 (2022).
- [39] Okoth, C., Cavanna, A., Santiago-Cruz, T. & Chekhova, M. V. Microscale generation of entangled photons without momentum conservation. *Phys. Rev. Lett.* **123**, 263602 (2019).
- [40] Kumar, N. *et al.* Second harmonic microscopy of monolayer MoS₂. *Phys. Rev. B* **87**, 161403 (2013).
- [41] Janisch, C. *et al.* Extraordinary second harmonic generation in tungsten disulfide monolayers. *Sci. Rep.* **4**, 5530 (2014).
- [42] Shi, J. *et al.* 3R MoS₂ with broken inversion symmetry: A promising ultrathin nonlinear optical device. *Adv. Mater.* **29**, 1701486 (2017).
- [43] Qin, B. *et al.* Interfacial epitaxy of multilayer rhombohedral transition-metal dichalcogenide single crystals. *Science* **385**, 99–104 (2024).
- [44] Qi, J. *et al.* Stacking-controlled growth of rBN crystalline films with high nonlinear optical conversion efficiency up to 1%. *Adv. Mater.* **36**, 2303122 (2024).
- [45] Ma, C. *et al.* Strong chiroptical nonlinearity in coherently stacked boron nitride nanotubes. *Nat. Nanotechnol.* (2024).
- [46] McKenna, T. P. *et al.* Ultra-low-power second-order nonlinear optics on a chip. *Nat. Commun.* **13**, 4532 (2022).

- [47] Willner, A. E., Khaleghi, S., Chitgarha, M. R. & Yilmaz, O. F. All-optical signal processing. *J. Lightwave Technol.* **32**, 660–680 (2014).
- [48] L. Chang *et al.* Second order nonlinear photonic integrated platforms for optical signal processing. *IEEE J. Sel. Top. Quantum Electron.* **27**, 1–11 (2021).
- [49] Yan, Q. *et al.* Ambient degradation anisotropy and mechanism of van der Waals ferroelectric NbOI₂. *ACS Appl. Mater. Interfaces* **16**, 9051–9059 (2024).
- [50] Zhang, S.-Y. *et al.* Molecule-based nonlinear optical switch with highly tunable on-off temperature using a dual solid solution approach. *Nat. Commun.* **11**, 2752 (2020).
- [51] Yang, Y.-C. *et al.* Inorganic solid-state nonlinear optical switch with a linearly tunable T_c spanning a wide temperature range. *Angew. Chem. Int. Ed.* **62**, e202301404 (2023).
- [52] Sun, Z., Martinez, A. & Wang, F. Optical modulators with 2D layered materials. *Nat. Photon.* **10**, 227–238 (2016).
- [53] Li, T. *et al.* Epitaxial growth of wafer-scale molybdenum disulfide semiconductor single crystals on sapphire. *Nat. Nanotechnol.* **16**, 1201–1207 (2021).
- [54] Hong, C. *et al.* Inclined ultrathin Bi₂O₂Se films: A building block for functional van der Waals heterostructures. *ACS Nano* **14**, 16803–16812 (2020).
- [55] Mennel, L. *et al.* Optical imaging of strain in two-dimensional crystals. *Nat. Commun.* **9**, 516 (2018).
- [56] Mennel, L., Paur, M. & Mueller, T. Second harmonic generation in strained transition metal dichalcogenide monolayers: MoS₂, MoSe₂, WS₂, and WSe₂. *APL Photonics* **4**, 034404 (2018).
- [57] Xu, R. *et al.* Strain-induced room-temperature ferroelectricity in SrTiO₃ membranes. *Nat. Commun.* **11**, 3141 (2020).
- [58] Chen, W., Gui, X., Yang, L., Zhu, H. & Tang, Z. Wrinkling of two-dimensional materials: Methods, properties and applications. *Nanoscale Horiz.* **4**, 291–320 (2019).
- [59] Dou, W. *et al.* Interfacial mechanical properties of double-layer graphene with consideration of the effect of stacking mode. *ACS Appl. Mater. Interfaces* **10**, 44941–44949 (2018).
- [60] Li, Z. *et al.* Efficient strain modulation of 2D materials via polymer encapsulation. *Nat. Commun.* **11**, 1151 (2020).
- [61] Hohenberg, P. & Kohn, W. Inhomogeneous electron gas. *Phys. Rev.* **136**, B864–B871 (1964).
- [62] Kohn, W. & Sham, L. J. Self-consistent equations including exchange and correlation effects. *Phys. Rev.* **140**, A1133–A1138 (1965).
- [63] Kresse, G. & Hafner, J. *Ab initio* molecular dynamics for liquid metals. *Phys. Rev. B* **47**, 558–561 (1993).
- [64] Kresse, G. & Furthmüller, J. Efficiency of *ab initio* total energy calculations for metals and semiconductors using a plane-wave basis set. *Comput. Mater. Sci.* **6**, 15–50 (1996).
- [65] Becke, A. D. Density-functional exchange-energy approximation with correct asymptotic behavior. *Phys. Rev. A* **38**, 3098–3100 (1988).
- [66] Langreth, D. C. & Mehl, M. J. Beyond the local-density approximation in calculations of ground-state electronic properties. *Phys. Rev. B* **28**, 1809–1834 (1983).
- [67] Perdew, J. P., Burke, K. & Ernzerhof, M. Generalized gradient approximation made simple. *Phys. Rev. Lett.* **77**, 3865–3868 (1996).
- [68] Marzari, N., Mostofi, A. A., Yates, J. R., Souza, I. & Vanderbilt, D. Maximally localized Wannier functions: Theory and applications. *Rev. Mod. Phys.* **84**, 1419–1475 (2012).
- [69] Ibañez-Azpiroz, J., Tsirkin, S. S. & Souza, I. *Ab initio* calculation of the shift photocurrent by Wannier interpolation. *Phys. Rev. B* **97**, 245143 (2018).
- [70] Garcia-Goiricelaya, P., Krishna, J. & Ibañez-Azpiroz, J. Including many-body effects into the Wannier-interpolated quadratic photoresponse tensor. *Phys. Rev. B* **107**, 205101 (2023).
- [71] Pizzi, G. *et al.* Wannier90 as a community code: New features and applications. *J. Phys.: Condens. Matter* **32**, 165902 (2020).